

Supercontinuum methane ranging based on boundary-feature triangulation

Yu-Jie Mao(毛宇杰), Kun-Yang Wang(王坤阳), Yue Lai(赖月), Shi-Qing Xu(徐时清)
Citation: Chin. Phys. B. 35, 094203 (2026). DOI: 10.1088/1674-1056/ae1b7b |
CSTR: 32038.14.CPB.ae1b7b
http://cpb.iphy.ac.cn; http://iopscience.iop.org/cpb

What follows is a list of articles you may be interested in

A cladding-pumping based power-scaled noise-like and dissipative soliton pulse fiber laser

Zhiguo Lv(吕志国), Hao Teng(滕浩), Zhiyi Wei(魏志义)
Chin. Phys. B. 32, 024207 (2023). DOI: 10.1088/1674-1056/ac8f3e

Numerical investigation of the nonlinear spectral broadening aiming at a few-cycle regime for 10 ps level Nd-doped lasers

Xi-Hang Yang(杨西杭), Fen-Xiang Wu(吴分翔), Yi Xu(许毅), Jia-Bing Hu(胡家兵), Pei-Le Bai(白培乐), Hai-Dong Chen(陈海东), Xun Chen(陈洵), Yu-Xin Leng(冷雨欣)
Chin. Phys. B. 31, 094206 (2022). DOI: 10.1088/1674-1056/ac685e

High power supercontinuum generation by dual-color femtosecond laser pulses in fused silica

Saba Zafar, Dong-Wei Li(李东伟), Acner Camino, Jun-Wei Chang(常峻巍), Zuo-Qiang Hao(郝作强)
Chin. Phys. B. 31, 084209 (2022). DOI: 10.1088/1674-1056/ac46be

All polarization-maintaining Er:fiber-based optical frequency comb for frequency comparison of optical clocks

Pan Zhang(张攀), Yan-Yan Zhang(张颜艳), Ming-Kun Li(李铭坤), Bing-Jie Rao(饶冰洁), Lu-Lu Yan(闫露露), Fa-Xi Chen(陈法喜), Xiao-Fei Zhang(张晓斐), Qun-Feng Chen(陈群峰), Hai-Feng Jiang(姜海峰), Shou-Gang Zhang(张首刚)
Chin. Phys. B. 31, 054210 (2022). DOI: 10.1088/1674-1056/ac40f6

Design and fabrication of GeAsSeS chalcogenide waveguides with thermal annealing

Limeng Zhang(张李萌), Jinbo Chen(陈锦波), Jierong Gu(顾杰荣), Yixiao Gao(高一骁), Xiang Shen(沈祥), Yimin Chen(陈益敏), Tiefeng Xu(徐铁峰)
Chin. Phys. B. 30, 034210 (2021). DOI: 10.1088/1674-1056/abd757

Supercontinuum methane ranging based on boundary-feature triangulation

Yu-Jie Mao(毛宇杰)[1], Kun-Yang Wang(王坤阳)[1,†], Yue Lai(赖月)[2], and Shi-Qing Xu(徐时清)[1]

[1] *Key Laboratory of Rare Earth Optoelectronic Materials and Devices of Zhejiang Province, Institute of Optoelectronic Materials and Devices, China Jiliang University, Hangzhou* 310018, *China*

[2] *Zhejiang University MingTrun Technology Co., Ltd., Hangzhou* 310030, *China*

(Received 16 September 2025; revised manuscript received 30 October 2025; accepted manuscript online 5 November 2025)

Accurate localization of methane leaks is important for environmental monitoring and safety. However, existing concentration measurement methods often cannot provide both high precision and distance information at the same time. This study proposes and experimentally tests a triangulation method that uses a supercontinuum light source and the plume's boundary features. The method leverages methane absorption in the 1630–1700 nm band, detects quick absorption changes at the plume edge, and uses triangulation geometry to find the leak source. On the same test platform, we compared this method with baseline triangulation and scanning–ranging techniques. The boundary-feature triangulation kept the measurement error between +0.1 cm and +1.0 cm, with an average error of about 0.41 cm, much better than the baseline method (average: 1.49 cm) and scanning method (some points up to 1.7 cm). The method shows fast response, good linearity, and concentrated errors, making it suitable for quick and reliable on-site methane leak localization and monitoring.

Keywords: supercontinuum laser, methane detection, triangulation ranging

PACS: 42.79.Qx, 07.07.Df, 42.68.Wt

DOI: 10.1088/1674-1056/ae1b7b **CSTR:** 32038.14.CPB.ae1b7b

1. Introduction

Methane (CH_4) is one of the largest greenhouse gases and plays a key role in driving climate warming and extreme weather. Although many countries have stepped up source control and emission reduction efforts in recent years and human-caused emissions have slowed, natural variability from wetlands and leaks during fossil fuel production remains highly uncertain.[1–3] Field studies of US oil and gas systems estimate annual CH_4 emissions at 13 ±2 Tg, roughly 2.3% of that year's natural gas production, an estimate nearly 60% higher than official US Environmental Protection Agency figures, suggesting that traditional accounting methods may underestimate true emissions.[4] CH_4 not only poses significant threats to global climate change but also presents potential risks to industrial safety and public health.[5] Therefore, developing efficient and precise methane leak detection technologies is of paramount importance.

Owing to its advantages of non-contact and long-range detection, remote sensing technology has become a research hotspot in the field of CH_4 leak detection and monitoring. These technologies can penetrate complex environmental obstacles, enabling rapid scanning across extensive areas, thereby enhancing the efficiency and coverage of leak detection.[6] Remote sensing techniques for CH_4 detection can be divided into two main categories: passive and active. Passive methods (such as hyperspectral and thermal imaging) rely on ambient radiation and are well suited for wide-area surveys from satellites, aircraft, or drones. They offer large spatial coverage but are sensitive to weak absorptions and background interference, which limits their quantitative accuracy.[7,8] By contrast, active methods use an emitted light source, and common examples are lidar approaches (DIAL, imaging lidar, and scanning lidar). The lidar approaches are instrumental in detecting and profiling CH_4 plumes. Overall, active methods offer advantages in sensitivity and temporal resolution but at the cost of greater system complexity, higher expense, and increased sensitivity to aerosols and visibility.[9–11] Passive methods trade lower sensitivity for easier deployment and wider coverage. Therefore, designing an operational CH_4 monitoring strategy requires a balanced choice among coverage, sensitivity, timeliness, and engineering feasibility.[12]

As a subset of active methods, laser-based remote sensing shows promise for CH_4 leak detection because it combines fast response, flexible field deployment, and relative robustness to environmental factors.[13] Recent studies have advanced concentration measurement performance. Duan *et al.* combined a 1654 nm distributed-feedback laser with a multichannel gas cell and used a mix of first-order modulation and second-harmonic normalization to push the detection limit down to 0.32 ppm while keeping the response time at around 1 s.[14] Ma *et al.* developed a fiber-optic multipoint sensor that detects CH_4 on-site in real time with a fast response. It of-

†Corresponding author. E-mail: wangky@cjlu.edu.cn

© 2026 Chinese Physical Society and IOP Publishing Ltd. All rights, including for text and data mining, AI training, and similar technologies, are reserved.

fers multipoint coverage, high stability, and easy deployment and scalability.[15] Zheng *et al*. proposed a compact dual-gas sensor that combines OA-ICOS with frequency-division-multiplexed WMS to simultaneously measure C_2H_2 and CH_4, achieving sub-ppm sensitivity and low noise.[16] Wang *et al*. developed a portable noncooperative-path remote sensing system that reconstructs CH_4 vertical concentration profiles from path-integrated measurements. Its path sensitivity reached 3.59 ppm·m, broadening scenarios where quantitative remote sensing can be applied.[17] Although these studies have made concentration measurement mature, they still lack distance localization capability. Without distance detection, it is difficult to pinpoint the exact location of CH_4. To precisely pinpoint leak sources in complex environments, further work on ranging methods is needed.

Laser ranging techniques can be grouped into three methods: time-of-flight (TOF), phase-difference (PD), and triangulation-based (TB) methods. The TOF method calculates distance from the round-trip time of laser pulses.[18] It works well for kilometer-scale ranges but imposes very high demands on pulse width and the receiver's time resolution; tiny timing errors can cause meter-level distance errors. The PD method compares the phase of a continuously modulated sine-wave signal between emission and return to achieve sub-millimeter precision.[19] However, its maximum range is limited by phase wrapping; therefore, there is a trade-off between accuracy and measurable distance. The TB method takes a different approach; if the baseline between emitter and receiver is known, measuring the outgoing and incoming angles forms a spatial triangle, and simple trigonometry gives the range. This method has a simpler hardware setup and fast response, making it well suited for short-range to mid-range handheld or embedded systems. In real-world applications, all three methods face physical limits (insufficient source brightness, limited output power, and beam divergence), which together restrict achievable ranging accuracy.

Supercontinuum (SC) lasers can produce a continuous, high-brightness, high-power spectrum with very small beam divergence across hundreds to thousands of nanometers. This wide spectral coverage makes them well suited for monitoring multiple greenhouse gases at once and for measuring species concentrations in complex multiphase flows.[20,21] Eslami *et al*. paired a high-repetition-rate mid-infrared supercontinuum with a 30 m multipass cell and synchronous demodulation, achieving methane sensitivity of tens of ppbv per root Hertz and about a fivefold improvement over baseband detection.[22] Adamu *et al*. focused on the 1480–1700 nm band and demonstrated fast responses to industrial gases, such as ammonia and CH_4. They showed that the source had good selectivity and long-term stability in online operation.[23] Moving into the mid-infrared, Bizot *et al*. used a thulium-pumped SC source to perform all-fiber absorption spectroscopy near 7.7 μm absorption peak and pushed the detection limit down to 20 ppm.[24] Blume and Wagner built a broadband supercontinuum absorption spectrometer for combustion diagnostics and reported methane measurements consistent with reference methods.[25] Because SC lasers cover multiple CH_4 absorption bands, they also open new possibilities for multi-wavelength, simultaneous ranging and concentration measurements.

To address the challenge of locating CH_4 leaks and meeting ranging requirements, this study proposes a boundary-feature triangulation (BFT) method based on the edge features of CH_4 plumes. It uses an SC laser to capture the momentary change in absorption at the plume edge and combines these measurements with geometric algorithms. To assess feasibility, this study evaluated this approach on the same experimental platform with two classic methods: baseline triangulation (BT), which relies on a fixed baseline and known emitter–receiver geometry, and scanning ranging (SR), which adds active multi-angle scanning to expand coverage. Both were also implemented with the SC laser for CH_4 leak ranging. Using the unified testbed, we ran repeated trials on simulated leak targets at different distances and performed a systematic comparison of the three methods in terms of measurement accuracy and stability, providing solid experimental data to select the best ranging scheme.

2. Program design

2.1. CH_4 absorption spectrum

Line-by-line HITRAN simulations were performed for CH_4, H_2O, and CO_2, and the spectra were compared. The simulations indicate that methane exhibits significant absorption peaks in both the near-infrared (NIR) and mid-infrared (MIR) regions. The intensity of the main absorption peak in the NIR region was approximately 1.5, whereas it was around 40 in the MIR region. Although MIR transitions are stronger and enable ultralow detection limits, MIR supercontinuum needs complex pumping, specialty nonlinear fibers, and cooled detectors. It is costly and prone to optical saturation over a typical path. In contrast, NIR supercontinuum uses mature pump lasers and robust silica fibers with inexpensive InGaAs detectors, delivers higher output power and beam quality, and is far less prone to saturation, making it more suitable for longer path detection. It is substantially cheaper and more reliable for field deployment.

As shown in Fig. 1, the NIR region was analyzed. The simulations were carried out under the following standard experimental conditions: $T = 296$ K and $p = 1$ atm, with background concentrations $H_2O \approx 1.0\%$ (volume mixing ratio) and $CO_2 \approx 420$ ppm, and CH_4 concentration $\approx 1.0\%$. One band lies between 1300 nm and 1700 nm. Inside that, the 1630–

1700 nm region is notable; a dense, strong absorption cluster near 1650 nm stands out. Its lines are well organized, the band width is moderate, and it has little interference from other gases, which makes it ideal for extracting weak signals. Under the path length and high-concentration injection conditions, CH_4 dominates the measured absorption, whereas H_2O and CO_2 produce only minor overlaps. Thus, the principal spectral features in the measurements are attributable to CH_4. By contrast, the 1300–1450 nm region is broader but much sparser. The integrated absorption of its main peaks is only about 10%–30% of the strength of the 1650 nm peaks. The weaker scattered peaks in this range often have long wings or overlap with each other, making peak analysis harder. This band is also more affected by other gases; therefore, the background noise level is higher and the useful signal is effectively reduced in real measurements.

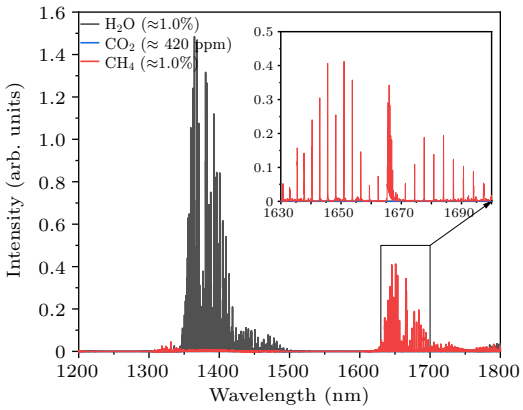


Fig. 1. CH_4 absorption spectrum simulated using HITRAN under standard experimental conditions ($T = 296$ K and $p = 1$ atm) with background concentrations $H_2O \approx 1.0\%$ (volume mixing ratio) and $CO_2 \approx 420$ ppm. CH_4 concentration $\approx 1.0\%$.

The 1630–1700 nm band meets the theoretical needs for high-precision ranging and offers clear engineering advantages, making it the core choice for CH_4 leak distance detection in this study.

2.2. Boundary-feature triangulation method

2.2.1. Experimental systems and devices

In the experiment, a supercontinuum laser (Precilasers; 20P011231) was chosen as the light source. This laser emits a high-brightness, very low-noise continuous spectrum. Table 1 lists the supercontinuum laser parameters. The laser spectrum (450–2400 nm) fully covers the 1630–1700 nm detection band. Simultaneous multiline capture enables multiline retrieval and a redundancy-based triggering scheme, which improves measurement stability and reliability under complex atmospheric conditions. The spectrometer (YOKOGAWA; AQ6375) used here has a minimum detectable pulse width of 50 μs and therefore cannot resolve the pulse-level spectral lines of the supercontinuum. Therefore, the measured spectrum is consequently the superposition of many components and appears continuous rather than as discrete narrow lines.

Table 1. Parameters of the supercontinuum laser.

Parameter	Data
Pulse width	10 ps
Pulse repetition frequency	4.88 MHz
Spectral coverage range	450–2400 nm
Maximum output power	1.1 W
Maximum single-pulse energy	225 nJ
Divergence angle	< 2 mrad
Power stability	$< 1\%$

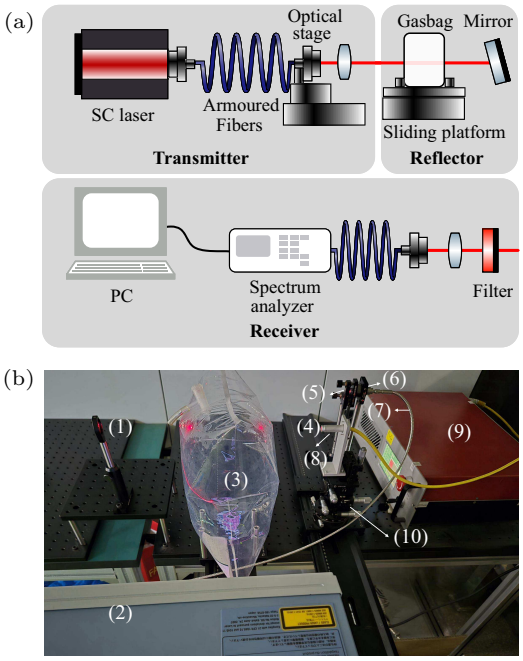


Fig. 2. (a) System diagram of the BFT method. (b) Physical setup: (1) flat mirror, (2) spectrometer, (3) gas bag, (4) sliding rail, (5) optical filter, (6) objective lens, (7) armored optical fiber, (8) beam collimator, (9) supercontinuum laser, and (10) six-dimension adjustment mount.

Figure 2 shows the schematic of the BFT system, which is made up of three linked parts: a transmitter, a reflector, and a receiver. The transmitter uses the supercontinuum laser. The output is repeatedly aligned using an adjustable beam collimator (Bocic; OM311) and a six-dimension adjustment mount (Daheng Optic; GCM 930602M) to produce a parallel, speckle-free continuous spectrum in the near-infrared. The CH_4 sample module sits at the center of the test platform on a horizontal sliding rail with a scale. A 5 L gas bag containing 99% pure CH_4 (30 cm×35 cm) is mounted on the rail; its horizontal position can be read directly from the scale, allowing millimeter-level control of the bag location. In the experiments, CH_4 gas bags were used to generate controlled and clearly observable absorption signals, simulating leakage conditions for experimental platform validation. At the far right, the reflector module uses a high-reflectivity flat mirror (Union Optic; MAG0125) to stably direct the beam that passes through the sample toward the receiver. The receiver first removes stray light with an optical filter (NMOT; BP-1653nm) mounted on a mirror mount (GU Optics; OM206B). An objective lens focuses the beam into an armored optical fiber (XiN-

RAY; SIH600/660-22A), which delivers the light to a high-resolution spectrometer for real-time spectral acquisition. The three modules operate together as a closed loop from emission to detection, forming a highly linear channel capable of high-precision ranging. On the same experimental platform and using identical hardware, two ranging methods (BT and SR methods) were used for target localization. The deviations between the measured and true distances were compared to highlight the differences in their accuracy and stability.

2.2.2. Principle of the experiment

Unlike static ranging methods, the BFT method uses a fixed triangular setup formed by a laser beam and a mirror. It dynamically captures subtle changes in the edge contour of a moving gas bag and calculates the precise position of the target in motion through trigonometric geometry.

The specific principle is illustrated in Fig. 3. In the system, the laser emitter (L), mirror (M), and receiver (S) form a fixed triangular measurement frame, denoted as LMS. The angle between the emitted laser path and reflected path is θ, and the baseline distance between the mirror and laser (LM) is d. When a CH_4 gas bag moves through this area at a speed v, its trajectory forms an angle φ with the emitted laser axis. The moving gas bag intersects both the emitted and reflected laser paths at two points (A and B). Using the known values of d, θ, and φ, the distances from the laser to the edges of the gas bag (L_A and L_B) can be instantly calculated through trigonometric relations. Reference distances L_{A0} and L_{B0} were obtained by direct measurement using a calibrated ruler with a stated resolution of 0.5 mm. Consequently, we adopted an uncertainty of ± 0.5 mm for these baseline distances. The angle φ (defined between the emitted beam and the horizontal sliding guide beneath the gas bag) was determined with a handheld protractor. A conservative reading uncertainty of $\pm 1^\circ$ was assumed to account for alignment and readout errors. These instrument uncertainties were propagated through trigonometric relations used to calculate the path lengths L_A and L_B and yield uncertainty bounds for the edge positions. This method preserves the geometric rigor of baseline triangulation while also enabling millisecond response and millimeter resolution through continuous contour tracking, significantly enhancing positioning robustness and accuracy for dynamic leakage monitoring.

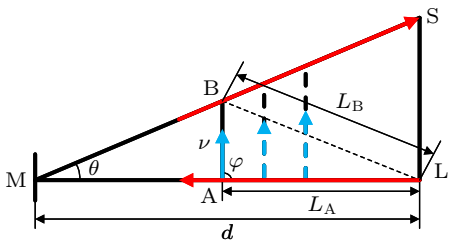


Fig. 3. Principle diagram of the BFT method.

When the target moves at an angle φ relative to the emission direction, the expression for the distance L_A is

$$L_A = d + \frac{v_0 \Delta t \cdot \cos\varphi \cdot (\tan\varphi - \tan\theta)}{\tan\theta}. \tag{1}$$

The distance L_B is given by

$$L_B = \left\{ (\cos\varphi \cdot v_0 \Delta t + LA)^2 + \left[\tan\theta \cdot \left(\cos\varphi \cdot v_0 \Delta t + \frac{v_0 \Delta t \cdot \cos\varphi \cdot (\tan\varphi - \tan\theta)}{\tan\theta} \right) \right]^2 \right\}^{\frac{1}{2}}. \tag{2}$$

As shown in Fig. 4, a classic BT system consists of three key components: emitter (A), reflector (P), and receiver (B). The baseline length L_{AB} remains constant after calibration. A laser is emitted at a known angle α, and when it hits the target, scattered or diffused light is produced. The receiver captures this returning signal and measures the angle β between the reflected light and the baseline. Using the known values of L_{AB}, α, and β, the precise distance between the target and the emitter (or receiver) can be quickly and reliably calculated using the sine rule.

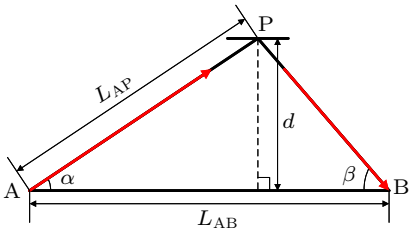


Fig. 4. Schematic diagram of the BT method.

In the SR method illustrated in Fig. 5, the laser is not fixed at one location. Instead, it moves sequentially to three predefined points (A, B, and C) in space. At each point, the emission angle is adjusted to θ_A, θ_B, and θ_C, respectively. After each emission, the system records the reflected signal and the corresponding emission angle. Finally, a least-squares fitting algorithm is used to combine these angle measurements and determine the optimal intersection point, thereby estimating the target's position.

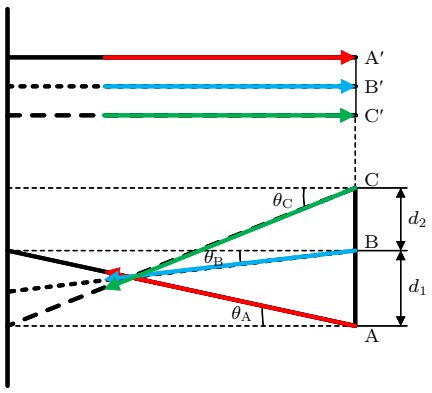


Fig. 5. Schematic diagram of the SR method.

2.2.3. Experimental process

During the experiment, a CH_4 gas bag was moved at a controlled speed along a pre-calibrated laser path. As it passed through the laser beam, a high-resolution near-infrared spectrometer continuously collected transmission data. This made it possible to clearly observe changes in absorption characteristics as the gas bag entered and exited the light path. The entire process can be divided into two distinct stages: baseline and triggered states.

Triggering was determined by manual visual inspection. During the experiment, the operator monitored the spectrometer display in real time while simultaneously visually observing and recording the gas-bag position. When a pronounced absorption peak emerged from the stable baseline and the timing of that spectral change coincided with the visually confirmed moment at which the gas-bag edge intersected the beam, the condition was designated as the triggered state, and the corresponding horizontal sliding rail reading was recorded. This operator-based criterion therefore provided an unambiguous temporal marker linking the spectral features to the physical position of the gas bag and ensured precise synchronization between spectral and motion data.

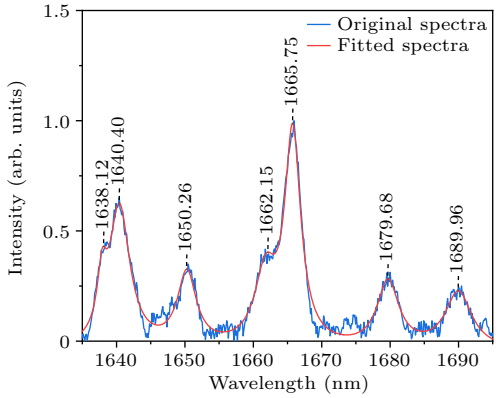


Fig. 6. Original absorption spectra and fitted spectra by multi-peak Lorentzian fit in the 1630–1700 nm range. The detected peak has been flagged.

In the baseline state, the spectrometer captures only the system's own response. The spectral curve shows no significant absorption features in the 1630–1700 nm range, confirming the absence of CH_4 interference. Once triggered, the edge of the gas bag gradually moves into the laser path. Some of the transmitted light is selectively absorbed by CH_4 molecules, causing distinct absorption peaks to appear in the characteristic wavelength band. To identify and track the CH_4 absorption features, we performed a multi-peak Lorentzian fit in Origin. Initial parameter estimates for the fit were assigned from the original spectra. As shown in Fig. 6, the fitted positions indicate a strongest feature at approximately 1665.75 nm, with additional moderate peaks near 1638.12 nm, 1640.40 nm, 1650.26 nm, 1662.15 nm, 1679.68 nm, and 1689.96 nm. The amplitudes of these peaks vary systematically as the gas bag moves through the beam, reflecting changes in the optical path overlap between the plume and laser. By monitoring the peaks in real time and combining them with the known geometric parameters of the system, the spatial movement of the edge of the gas bag can be accurately reconstructed. The use of multiple identifiable lines provides redundancy and improves robustness against local spectral interference.

Table 2 summarizes the readings from the BFT method when the CH_4 gas bag passed through point A (on the incident beam) and point B (on the reflected beam) on the calibrated sliding platform, along with the straight-line distance AB between these points. The table also includes the fixed baseline distance d between the laser emitter and mirror, which plays a key role in the subsequent distance calculation based on trigonometric functions.

The speed v of the gas bag often fluctuates slightly during movement owing to friction and platform inertia; therefore, using time intervals Δt directly may lead to inconsistency. Instead, we used linear displacement Δx (i.e., AB) between the two points as a substitute for $v\Delta t$ to simplify data acquisition. By combining the measured Δx with the known field angle θ (15°) and baseline length d, the instantaneous distances L_A and L_B can be quickly calculated. This approach reduces the dependency on highly precise time measurements under strictly constant speed and makes subsequent data processing more efficient and reproducible.

Table 2. Measurement parameters of the BFT method..

Measurement number	A location (mm)	B location (mm)	Δx (mm)	Distance d (cm)
1	130	320	190	130
2	129	301	172	130
3	129	288	159	130
4	130	275	145	130
5	130	262	132	130
6	125	270	145	140
7	126	272	146	145
8	127	274	147	150
9	124	271	147	155
10	128	272	144	160

2.3. Results

Table 3 presents the detailed results and error statistics from ten dynamic experiments using the BFT method to measure CH_4 gas bag. In each experiment, the system recorded the difference between the measured distance from the laser source to point A (L_{A1}) and the actual reference distance (L_A), denoted as $\Delta L_A = L_{A1} - L_A$. Similarly, the difference for point B, $\Delta L_B = L_{B1} - L_B$, was also obtained. Repeated measurements show that ΔL_A ranged from -0.9 cm to $+1.2$ cm, with a mean error of $+0.15$ cm and a standard deviation of 0.48 cm. Most deviations fell within 1.0 cm. For ΔL_B, the values varied

from +0.1 cm to +1.0 cm, with a mean error of +0.42 cm and a standard deviation of 0.27 cm. Most measurement errors did not exceed +0.8 cm.

Based on the above error analysis, the system maintains millimeter-level accuracy even under dynamic conditions. The errors are tightly clustered, and performance is highly consistent, fully meeting the dual requirements of high precision and reliability for CH_4 leakage monitoring.

Table 3. Distance measurement and error analysis of the BFT method.

Measurement number	L_{A0} (cm)	L_{A1} (cm)	ΔL_A (cm)	L_{B0} (cm)	L_{B1} (cm)	ΔL_B (cm)
1	60	59.1	−0.9	62	62.1	0.1
2	65	65.8	0.8	67	68.0	1.0
3	70	70.7	0.7	72	72.5	0.5
4	75	75.9	0.9	77	77.3	0.3
5	80	80.7	0.7	81	81.8	0.8
6	85	85.9	0.9	87	87.1	0.1
7	90	90.5	0.5	91	91.7	0.7
8	95	95.1	0.1	96	96.2	0.2
9	100	100.1	0.1	101	101.2	0.2
10	105	106.2	1.2	107	107.2	0.2

In this study, the measured and true values for both the BT and SR methods were strictly defined and compared. For the baseline method, the true distance is denoted as d_0 and the measured distance as d_1, with the error calculated as $\Delta d = d_1 - d_0$. For the scanning method, the true value is x_0 and the measured value is x_1, with error $\Delta x = x_1 - x_0$.

Table 4 shows the error distributions of both methods across multiple test points. In the BT method, Δd values ranged from as low as 0.5 cm to as high as 2.9 cm, with most errors falling between 0.6 cm and 2.1 cm. This suggests that the system may occasionally produce larger deviations under certain angle configurations. In contrast, the SR method demonstrated more stable performance: Δx varied from −1.4 cm to +1.7 cm, with most errors concentrated between −0.3 cm and +1.3 cm. This resulted in a smaller overall negative bias and tighter error distribution.

Table 4. Measurement results of the BT and SR methods.

Measurement number	d_0 (cm)	d_1 (cm)	Δd (cm)	x_0 (cm)	x_1 (cm)	Δx (cm)
1	60	60.8	0.8	60	59.7	–0.3
2	65	65.6	0.6	65	66.2	1.2
3	70	71.0	1.0	70	70.8	0.8
4	75	77.1	2.1	75	75.8	0.8
5	80	80.5	0.5	80	80.9	0.9
6	85	87.9	2.9	85	86.2	1.2
7	90	92.1	2.1	90	91.7	1.7
8	95	96.6	1.6	95	95.1	0.1
9	100	101.5	1.5	100	101.3	1.3
10	105	106.8	1.8	105	103.6	–1.4

By presenting the distance parameters, actual measurement results, and errors of the three ranging methods (BT, SR, and BFT) side by side, a direct and clear performance comparison can be made for CH_4 distance measurement tasks.

As shown in Fig. 7, the blue dotted line in the upper section indicates the preset reference values. In both BT and SR methods, the target distances increased from 60 cm to 105 cm in 5 cm increments. For BFT, point B increased from 62 cm to 107 cm, also at 5 cm intervals. The orange line tracks the actual measurements under the same experimental conditions. The BT method produced values ranging from 60.8 cm, 65.6 cm, and up to 106.8 cm. The SR method yielded the following results: 59.7 cm, 66.2 cm, and up to 103.6 cm. The BFT method recorded L_B values from 62.1 cm to 107.2 cm. The lower section uses yellow bars to show the error values, defined as the difference between the measured and reference values, and a green line connects these points to illustrate the variation in error across different measurement positions.

By comparing the three methods under the same experimental conditions, their error characteristics become clearly visible. The BT method shows the largest and most irregular fluctuations in error. Although the SR method exhibits smaller errors at most positions, it still occasionally produces negative deviations, and some points show relatively large positive errors. In contrast, the BFT method consistently keeps errors within ±1.0 cm at point B, demonstrating the most concentrated and stable performance.

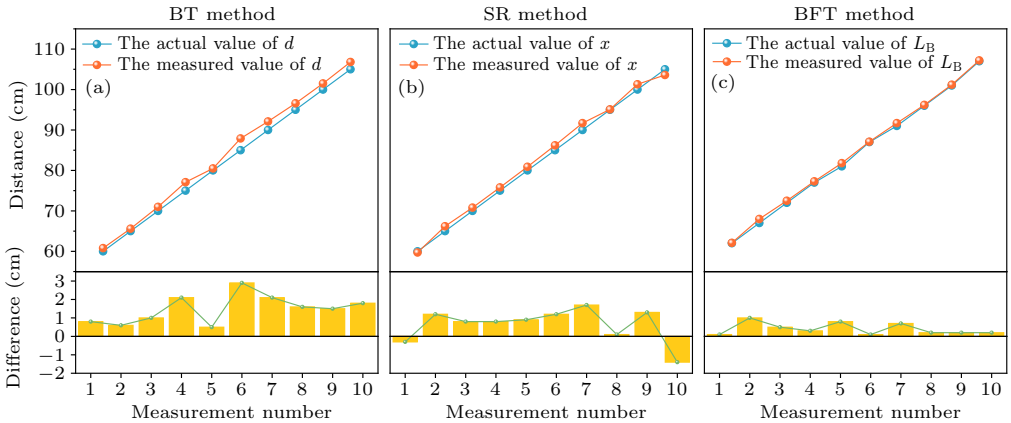


Fig. 7. Measured d values and deviation plot for (a) the BT method, (b) the SR method, and (c) the BFT method.

This comparison clearly demonstrates the strength of the BFT method in ensuring both measurement stability and positioning accuracy in dynamic ranging scenarios, providing strong support for real-time CH_4 leakage monitoring.

The measurement errors of the three key parameters (d, x, and L_B) from the three sets of experiments are presented together using a combined point-line graph (see Fig. 8). This visualization clearly shows the differences in positioning accuracy among the methods and facilitates observation of how accuracy evolves throughout the measurement process.

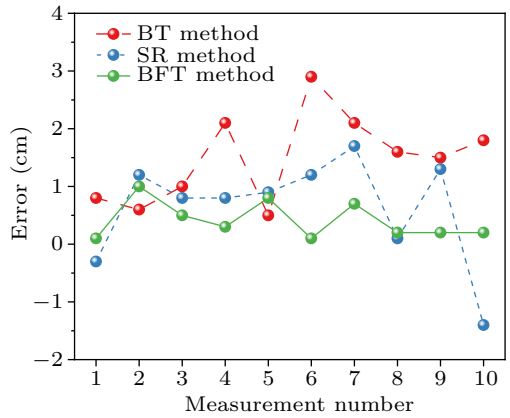


Fig. 8. Comparative error plots for the three experimental methods.

In the BT method (Fig. 9), the errors in measuring distance d are widely scattered, with a maximum deviation of up to 2.9 cm and an average error of about 1.49 cm. Multiple datasets indicate clear stability shortcomings in their basic positioning mechanism. This suggests that relying solely on BT may not meet high-precision measurement requirements in complex environments.

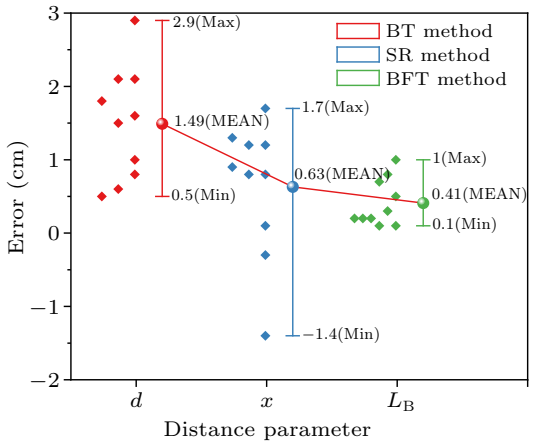


Fig. 9. Error ranges and mean values of the three experimental methods.

With the SR method, although most errors are controlled within 1.5 cm across multiple points, a few measurements still deviate up to 1.7 cm. Moreover, the error tends to increase nonlinearly with distance. This occurs because minor angle adjustments are magnified over longer distances, leading to more significant positioning inaccuracies. Thus, as the target moves farther away, angle control becomes increasingly critical for maintaining accuracy.

Notably, the error distributions for L_B in the BFT method are highly concentrated. All data points fall within a narrow range of 0.1–1 cm, with the average error firmly kept within ±0.5 cm. The maximum error does not exceed 1 cm, and deviations are tightly clustered with the smallest fluctuations, demonstrating the highest positioning accuracy. These results confirm the effectiveness of the improved ranging approach.

3. Discussion

The boundary-feature triangulation (BFT) method offers three practical advantages: fast single-shot broadband acquisition that captures multiple CH_4 lines simultaneously, redundancy across lines that increases robustness to local spectral interference, and a simple geometric triangulation step that converts temporal edge triggers into direct range estimates for moving plume boundaries. These strengths make BFT particularly suitable for rapid localization of transient leaks. At the same time, important limitations must be considered. The laboratory spectrometer used here is large and not easy to deploy in the field, and its finite spectral resolution makes it difficult to fully separate adjacent or overlapping absorption lines, increasing interference from atmospheric species, such as water vapor and carbon dioxide. Deformation of the moving gas bag causes blurring of the plume edge. Variability in temperature and humidity alters line strength and baseline.

To address these issues, we will adopt compact fiber-coupled spectrometers with dedicated high-resolution channels, replace or calibrate the gas bag with stiffer or controlled-release boundary sources and record high-speed imaging plus three-dimensional anemometry, and apply temperature–pressure–humidity (T–P–H)-conditioned lookup table corrections convolved with the instrument line shape and a formal uncertainty budget. Collectively, these measures are expected to reduce spectral bias, tighten trigger timing, and enhance the quantitative reliability of BFT localization in field conditions.

4. Conclusion

This study addresses the need for CH_4 leak distance measurement by introducing a BFT method based on plume edge detection, with BT and SR included as comparative methods. Using the same experimental platform, a rigorous comparison was conducted to evaluate the performance of the three methods in terms of accuracy and stability. In contrast, the BFT method combines laser scanning of the gas bag edge with variations in CH_4 absorption peaks, integrating the data into a geometric model. The experimental results show errors for L_B

between +0.1 cm and +1.0 cm. The method not only demonstrates excellent linear response but also maintains very low absolute error.

The limitations of the BFT method include bulky spectrometers, limited spectral resolution, gas bag deformation, and *T*–*P*–*H* variability. To address these, we will deploy compact spectrometers, rigid boundary sources, high-speed imaging, 3D anemometry, and *T*–*P*–*H*-conditioned corrections. These measures are expected to reduce spectral bias, improve trigger timing, and enhance the reliability of BFT localization in the field.

Overall, the optimized BFT method significantly enhances both measurement accuracy and stability, maintaining system-wide errors within a narrow interval and yielding the lowest mean error. Its consistency and suppression of fluctuation outperform those of the baseline and scanning methods, providing reliable data support for rapid detection and precise localization of CH_4 leaks in complex atmospheric environments.

Acknowledgements

This study was supported by the National Natural Science Foundation of China (Grant No. 42205144), the Baima Lake Laboratory Joint Funds of the Zhejiang Provincial Natural Science Foundation of China (Grant No. LBMHZ24F050002), and the Key Research and Development Project in Zhejiang Province (Grant No. 2024C03246).

References

[1] Saunois M, Martinez A, Poulter B, *et al*. 2025 *Earth System Science Data* **17** 1873
[2] Zhang Z, Zimmermann N E, Stenke A, Li X, Hodson E L, Zhu G, Huang C and Poulter B 2017 *Proc. Natl. Acad. Sci. USA* **114** 9647
[3] Tibrewal K, Ciais P, Saunois M, Martinez A, Lin X, Thanwerdas J, Deng Z, Chevallier F, Giron C, Albergel C, Tanaka K, Patra P, Tsuruta A, Zheng B, Belikov D, Niwa Y, Janardanan R, Maksyutov S, Segers A, Tzompa-Sosa Z A, Bousquet P and Sciare J 2024 *Commun. Earth Environ.* **5** 26
[4] Alvarez R A, Zavala-Araiza D, Lyon D R, *et al*. 2018 *Science* **361** 186
[5] Calderon J L, Sorensen C, Lemery J, Workman C F, Linstadt H and Bazilian M D 2022 *J. Environ. Manage.* **310** 114766
[6] Jongaramrungruang S, Matheou G, Thorpe A K, Zeng Z C and Frankenberg C 2021 *Atmos. Meas. Tech.* **14** 7999
[7] Rouet-Leduc B and Hulbert C 2024 *Nat. Commun.* **15** 3801
[8] Gorroño J, Varon D J, Irakulis-Loitxate I and Guanter L 2023 *Atmos. Meas. Tech.* **16** 89
[9] Barton-Grimley R A, Nehrir A R, Kooi S A, Collins J E, Harper D B, Notari A, Lee J, DiGangi J P, Choi Y and Davis K J 2022 *Atmos. Meas. Tech.* **15** 4623
[10] Zhang X, Zhang M, Bu L, Fan Z and Mubarak A 2023 *Remote Sens.* **15** 3239
[11] Kiemle C, Kawa S R, Quatrevalet M and Browell E V 2014 *J. Geophys. Res.: Atmos.* **119** 4365
[12] Cairo F, Di Liberto L, Dionisi D and Snels M 2024 *Remote Sens.* **16** 2788
[13] Erland B M, Thorpe A K and Gamon J A 2022 *Environ. Sci. Technol.* **56** 16567
[14] Duan W, Yan F, Wang Y, Zhang H, Ma L, Wen D, Wang W, Sheng G and Wang Q 2022 *Sensors* **22** 556
[15] Ma L, Liu X and Si G 2024 *Sensors* **24** 5031
[16] Zheng K, Zheng C, Yao D, Hu L, Liu Z, Li J, Zhang Y, Wang Y and Tittel F K 2019 *Analyst* **144** 2003
[17] Wang D, Li Y, Pu Y, Lv Y, Wang M, Yang H, Zhao X and Li D 2024 *Sensors* **24** 1307
[18] uliano Martins R, Marinov E, Youssef M A B, Kyrou C, Joubert M, Colmagro C, Gâté V, Turbil C, Coulon P M, Turover D, Khadir S, Giudici M, Klitis C, Sorel M and Genevet P 2022 *Nat. Commun.* **13** 5724
[19] Li N, Ho C P, Xue J, Lim L W, Chen G, Fu Y H and Lee L Y T 2022 *Laser & Photonics Reviews* **16** 2100511
[20] Krebbers R, Kempen K van, Harren F J M, Vasilyev S, Peterse I F, Lücker S, Khodabakhsh A and Cristescu S M 2024 *Opt. Express* **32** 14506
[21] Zorin I, Gattinger P, Ebner A and Brandstetter M 2022 *Opt. Express* **30** 5222
[22] Eslami Jahromi K, Nematollahi M, Pan Q, Abbas M A, Cristescu S M, Harren F J M and Khodabakhsh A 2020 *Opt Express* **28** 26091
[23] Adamu A I, Dasa M K, Bang O and Markos C 2020 *IEEE Sensors Journal* **20** 10591
[24] Bizot R, Tiliouine I, Désévédavy F, Gadret G, Strutynski C, Serrano E, Mathey P, Kibler B, Février S and Smektala F 2024 *APL Photon.* **9** 111303
[25] Blume N G and Wagner S 2015 *Opt. Lett.* **40** 3141